CGAN-ECT: Tomography Image Reconstruction from Electrical Capacitance Measurements Using CGANs

Wael Deabes
Computer Science Dep. in Jamoum,
Umm Al-Qura University, KSA
Computers and Systems Engineering Dep.,
Mansoura University, Egypt
wadeabes@uqu.edu.sa

Alaa E. Abdel-Hakim
Computer Science Dep. in Jamoum,
Umm Al-Qura University
Electrical Engineering Department
Assiut University
Assiut, Egypt, 71516
adali@uqu.edu.sa;
alaa.aly@eng.au.edu.eg

September 13, 2022

Abstract

Due to the rapid growth of Electrical Capacitance Tomography (ECT) applications in several industrial fields, there is a crucial need for developing high quality, yet fast, methodologies of image reconstruction from raw capacitance measurements. Deep learning, as an effective non-linear mapping tool for complicated functions, has been going viral in many fields including electrical tomography. In this paper, we propose a Conditional Generative Adversarial Network (CGAN) model for reconstructing ECT images from capacitance measurements. The initial image of the CGAN model is constructed from the capacitance measurement. To our knowledge, this is the first time to represent the capacitance measurements in an image form. We have created a new massive ECT dataset of 320K synthetic image-measurements pairs for training, and testing the proposed model. The feasibility and generalization ability of the proposed CGAN-ECT model are evaluated using testing dataset, contaminated data and flow patterns that are not exposed to the model during the training phase. The evaluation results prove that the proposed CGAN-ECT model can efficiently create more accurate ECT images than traditional and other deep learning-based image reconstruction algorithms. CGAN-ECT achieved an average image correlation coefficient of more than 99.3% and an average relative image error about 0.07.

Keywords CGAN · Tomography Systems · Image Reconstruction

1 Introduction

Tomography plays a crucial role in industrial fields, e.g. food industry, industrial tomography, biomedical [1], chemical, and pharmaceutical processes [2, 3], and non-destructive assessment of invisible objects in dams and flood embankments [4, 5]. The inner distribution of materials inside pipes is essential in such application domains. Electrical Tomography (ET) is an imaging technology that can provide such distributions in a form of cross-sectional images using non-invasive outer electrical measurements [6]. Capacitance is a proper electrical property that fits this purpose. The outer capacitance measurement can capture the variations in permittivity distributions of the inner materials. This is achieved by Electrical Capacitance Tomography (ECT). The ECT is an imaging modality that enjoys several advantages over other tomography modalities. Beside it is non-invasive and non-destructive, it is fast, inexpensive, and radiation hazards-free. Moreover, various electrical properties of diverse flow materials can be represented by ECT.

An ECT system contains in its core an array of capacitance sensors, along with a data acquisition hardware, and a post-processing unit, which is typically an imaging computer. Multiple exciting electrodes are evenly mounted around the imaged vessel in order to build up an ECT sensor [7], as shown in Fig. 1. With the aid of these sensors, the ECT system can determine the changes in the capacitance measurements due to variations of dialectic material
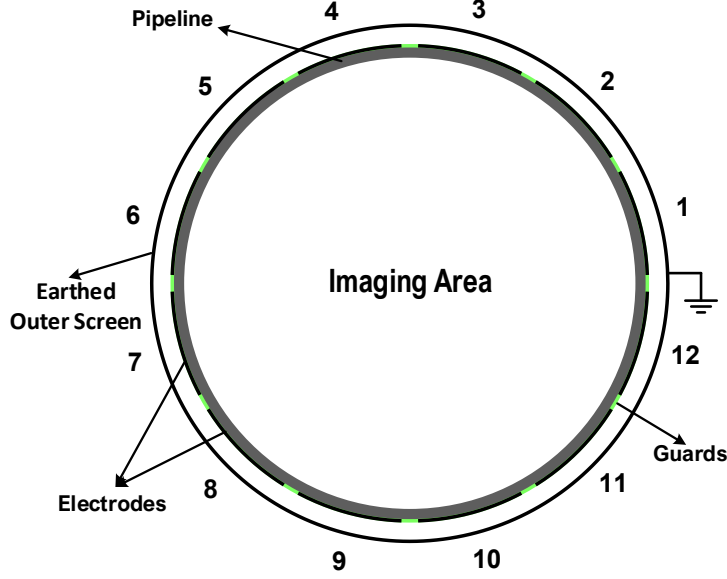
Figure 1: ECT sensor with 12 electrodes

distribution inside the imaging area. The collected measurements are used to build cross-sectional images representing the permittivity distribution. This process is called the inverse problem and is accomplished using image reconstruction algorithms [8, 9].

The ECT image reconstruction problem is being paid special interest in literature. This is due to its sophistication resulted from the non-linear relationship between the permittivity distribution and the measurements. Additionally, from a practical perspective, the choice of the optimal imaging method for a specific application is not straightforward.

The ECT image reconstruction process can be performed using non-iterative algorithms, e.g. Linear Back Projection (LBP) [10]; or iterative algorithms, e.g. Tikhonov regularization [11], Newton Raphson [12], and Iterative Landweber Method (ILM) [13]. Although the non-iterative methods are obviously fast and simple, their reconstructed images usually suffer from deformations. On the other side, iterative methods generate images with higher quality. However, they are computationally expensive. Therefore, they are more suitable for offline applications.

Machine Learning (ML), particularly Deep Learning (DL), methods showed up as the tools that can compromise the tradeoff between reconstructing high-quality images and computation efficiency. The ability of DL to map complex non-linear functions enables them to be endorsed by many domains [14]. Several attempts have been made to exploit ML in ECT. A non-linear image reconstruction approach was evolved using a conjoined Feed Forward Neural Network (FFNN) and analog Hopfield Network [15]. Deabes et al. [16], implemented a highly reliable (ECT-LSTM-RNN) model for industrial applications to predict the metal distribution during the Lost Foam Casting (LFC) process. Also, they developed a LSTM-Image Reconstruction (LSTM-IR) algorithm [17] to generate high quality ECT images. Zhu et a. [18] presented a forward, an inverse, permittivity prediction network in a deep neural network to reconstruct the object shape. For the improvement purposes of the reconstructed images of multiple different permittivity values in the sensing field, Zhu et al. added multi-level fusion layer to DL conventional methods [14]. In [19], an adversarial resolution enhancement (ARE-ECT) model was presented to reconstruct high-resolution images of inner distributions based on low-quality initial images. A Residual Autoencoder called (ECT-ResAE) was implemented in [20] to generate ECT images from modulated capacitance measurement images.

Despite the success achieved by such methods, they depend on small training datasets. This leads to generalization problems, which appears with never-seen capacitance vectors. So, generating large-scale ECT datasets for training, validation, and testing purposes along with and implementing new ML image reconstruction frameworks are essential for better generalization capabilities in extensive applications. In this paper, a DL framework called CGAN-ECT model for creating tomography images from capacitance measurements is developed. The model uses Conditional Generative Adversarial Networks (GAN) [21] with a UNet generator [22]. The GANs have yielded splendid results in many image generating tasks, such as photographs of human faces, image-to-image Translation, photograph editing, and others [23]. The inputs of the proposed CGAN-ECT model are the capacitance measurements after a modulation process converting it to a square matrix. The output is a reconstructed tomography image identifying all the objects inside the imaging area. The trained CGAN-ECT model is obviously fast since its forward operation mode. A large-scale dataset with $320k$

pairs has been created to train and test the proposed model. The proposed method yields more accurate images than other explicit approaches with a lower computational cost.
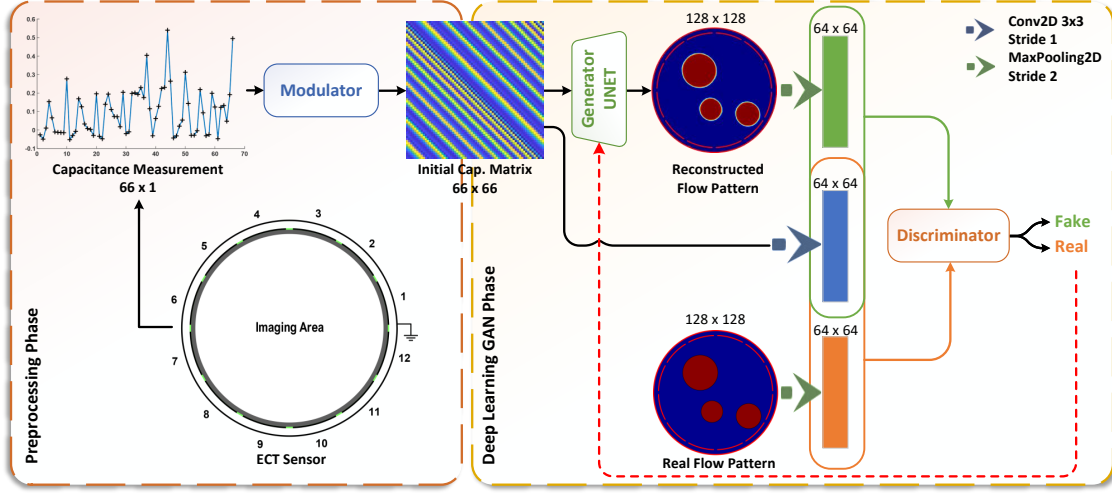

Figure 2: Architecture of CGAN-ECT model

2 CGAN-ECT Model Description

In ECT, the relationship between capacitance measurement readings and cross-sectional images is formulated as a two-way mapping problem. The forward problem is relatively the easier one. It is concerned by estimating the capacitance readings given cross-sectional data, as shown in Eq. 1.

$$C_{M \times 1} = S_{M \times N}(\varepsilon_0) \cdot G_{N \times 1} \qquad (1)$$

where S is the sensitivity matrix, which is the Jacobian of the capacitance with respect to pixels evaluated at ε_0 (the first permittivity distribution), N is the number of image's pixels, M is the number of sensor-pair readings. G is the permittivity distribution, and C is the calculated capacitance.

The inverse problem is simply estimating G given C. Obviously, the inverse problem is an ill-posed one. Therefore, the generated cross-sectional image is very sensitive to measurement errors [24]. The existing algorithms for the reverse problem usually suffer from quality or efficiency drawbacks. We propose the CGAN-ECT model to overcome these ECT related problems. The following subsections explain the main components of the proposed CGAN-ECT model, as shown in Fig. 2.

2.1 Modulator

The ECT capacitance sensor produces a 1×66 raw vector data, i.e. $M = 66$. If the sensor set is rotated CCW, another 1×66 vector is generated. This generated vector is rotate-right version of the first one. When this single step rotation is repeated, a matrix of 66×66 is generated. Such kind of sensor virtual rotation achieves the rotation-invariance property for the inner material distribution. In other words, the generated matrix is rotation invariant. This property is extremely crucial, specially for the case of asymmetric flow patterns. Rotation invariance achieves compactness of the input data with diverse poses of inner objects. Particularly, for an asymmetric flow pattern, a single matrix provides comprehensive readings regardless the relative placement of the sensors with respect to the inner pattern spatial orientation. The main objective of the modulator is to implement such readings augmentation. Specifically, it is responsible of generating the rotation-invariant initial capacitance matrix from a single vector reading. Algorithm 1 shows the operation of the modulator.

2.2 Generator

The spatial information of the inner material distribution is crucial in constructing the image of the flow pattern. Although traditional autoencoders are good in reconstructing such patterns, they cannot recover the spatial information

---

Algorithm 1 The modulator operation

procedure MODULATOR($C_{1 \times M}, C_{M \times M}$)
    $v \leftarrow C_{1 \times M}$
    $C_{M \times M} \leftarrow zeros(M, M)$

    for $i = 1 : M$ **do**
        $C_{M \times M}[i, :] \leftarrow [v]$
        $v \leftarrow rotate\_right(v, 1)$
    end for
    return $C_{M \times M}$
end procedure

---

contents with sufficient accuracy. UNet has been proven to cover this gap [22]. Therefore, we use UNet in the generator to construct the final flow pattern. We use 4 blocks in the encoder side, and 4 blocks in the decoder side. The size of the latent vector is 8. The initial modulated capacitance matrix of the input layer is concatenated with the generated image from final layer. Similarly, each input of the hidden layers in the decoder side is concatenated with the output of the corresponding layer from the encoder side.

2.3 CGAN Model

The core of the deep learning phase is a CGAN network [21]. The constructed flow patterns that are generated by the UNet generator, $G(C_{M \times M})$, work as the fake samples. The real samples, FP_r, are obtained from the synthetic image set, $\mathcal{FP}$, which are generated by the proposed synthetic generator described in section 3.1. The generated image from the generator, and the real image are passed through a maxpooling layer with 64 filters, while the initial modulated capacitance matrix is convoluted by a Conv2D layer with a 3×3 mask and a stride of 1 to generate a downsized image of size equals 64×64. Both real and fake samples are conditioned by that produced 64×64 image, as shown in Eq. 2.

$$
\begin{aligned}
G^* = \arg \min_G \max_D (& \underset{FP_r \in \mathcal{FP}}{\mathbb{E}}[\log(D(FP_r | C_{M \times M}))] + \\
& \underset{C_{M \times M} \in \mathcal{CM}}{\mathbb{E}}[\log(1 - D(G(C_{M \times M}) | C_{M \times M}))])
\end{aligned}
\tag{2}
$$

where $\mathcal{CM}$ is the set of capacitance measurement matrices.

3 Experimentation

3.1 Experimental Setup and ECT Dataset

We have implemented a Matlab GUI software package to realize different configurations of ECT sensors. By solving the ECT forward problem, various flow patterns can be simulated, and their corresponding capacitance measurements are generated. Accordingly, an extensive ECT benchmark dataset has been developed to train and test the proposed algorithm. The dataset consists of $320k$ samples, each one is a pair of an actual permittivity distribution vector, and its corresponding capacitance measurements modulated matrix. The size of the actual flow pattern is 128×128, while the modulated matrix is 66×66. The ECT sensor consists of 12 electrodes as shown in Fig. 1. The sensor pipe is made from PVC material with a relative permittivity of 2. The diameter and the thickness of the pipe are $93mm$ and $2.5mm$, respectively. The electrodes are separated by gaps of 4°, and the span angle of each electrode is 26°. The dataset contains 9 different flow patterns: $10k$ ring patterns, annular with $20k$ patterns, $10k$ stratified patterns, $1 - 3$ circular bars with $140k$ patterns, and $140k$ patterns of $1 - 3$ square bars, as shown in Fig. 3. The low permittivity phase is air with value 1, and the high phase is plastic particles with permittivity of 4. the physical specifications of every pattern are assigned stochastically. For instance, the ring's width for annular flow is assigned to a random variable between 10% and 95% of its radius. The height of the stratified flow is randomly set between 5% and 95% of the diameter. The number of bars varies from 1 to 3. Additionally, for testing, the trained CGAN-ECT model, a real ECT system is used to measure real capacitance data.

3.2 Evaluation Metrics

In the ECT inverse problem, usually the image quality, and reconstruction algorithm's performance are evaluated using two common metrics: the relative Image Error (IE) and Correlation Coefficient (CC) between the actual and the
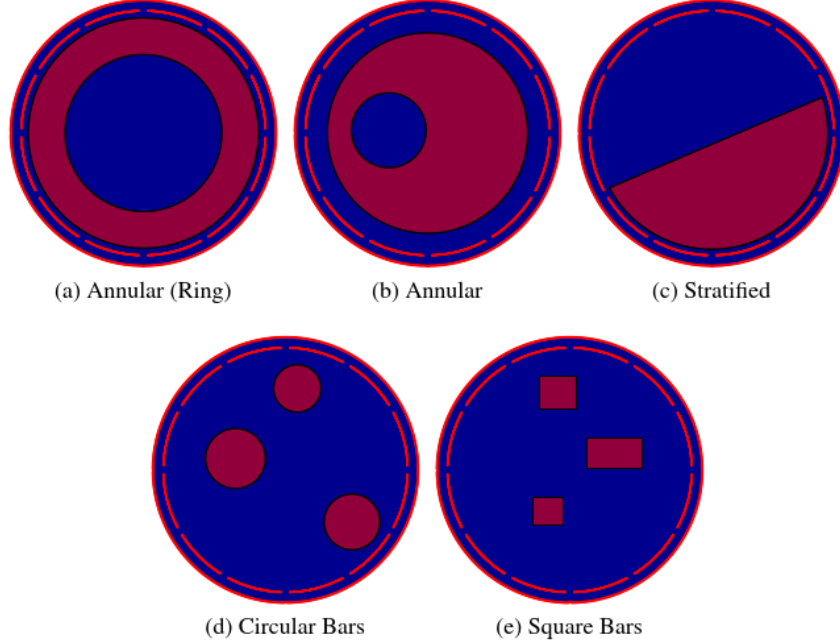
Figure 3: Samples of different flow patterns

reconstructed flow patterns [8]. The relative IE is defined as shown in Eq. 3.

$$IE = \frac{||G - G^*||_2}{||G||_2} \tag{3}$$

where G^* represents the predicted permittivity distribution from the generator network of CGAN-ECT image reconstruction model, and G represents the original material distribution.

The CC, which is shown in Eq. 4, measures how similar the reconstructed image is to the actual flow distribution.

$$CC = \frac{\sum_{i=1}^{N}(G_i - \bar{G})(G_i^* - \bar{G}^*)}{\sqrt{\sum_{i=1}^{N}(G_i - \bar{G})^2 \sum_{i=1}^{N}(G_i^* - \bar{G}^*)^2}} \tag{4}$$

where G is the actual permittivity distribution of the test object, G^* is the reconstructed permittivity distribution, and $\bar{G}$ and $\bar{G}^*$ are the mean values of G and G^*, respectively. $N = 16384$ is the number of pixels in the imaging area.

The training and testing process of the CGAN-ECT model is implemented in Python on TensorFlow machine learning platform [25], and Keras deep learning API [26]. When the proposed model is tested, the input is the modulated capacitance matrix, while the reconstructed permittivity flow pattern is the output. Since the testing set consists of $96k$ samples, therefore the performance is measured based on the mean values of these two metrics. Smaller relative IE and larger CC correspond to better performance.

3.3 Evaluation Results

The overall network's performance of the proposed model is verified based on the reconstruction results of the testing dataset. The more comprehensive the data simulation, the stronger the generalization performance of the model after training. Therefore, the generalization ability of the proposed model is tested by using testing dataset, generated phantoms, which are not included in the training dataset, and real experimental data.

3.3.1 Qualitative Results on Simulation Test Dataset

Practically, a simulation testing dataset, which had not been exhibited to the network during the training process, is used to verify the reconstruction ability of the proposed CGAN-ECT model. Typically, the ECT dataset containing $320k$ pairs is divided into 70% ($224k\ pairs$) for training, and 30% ($96k\ pairs$) for testing. The training and testing
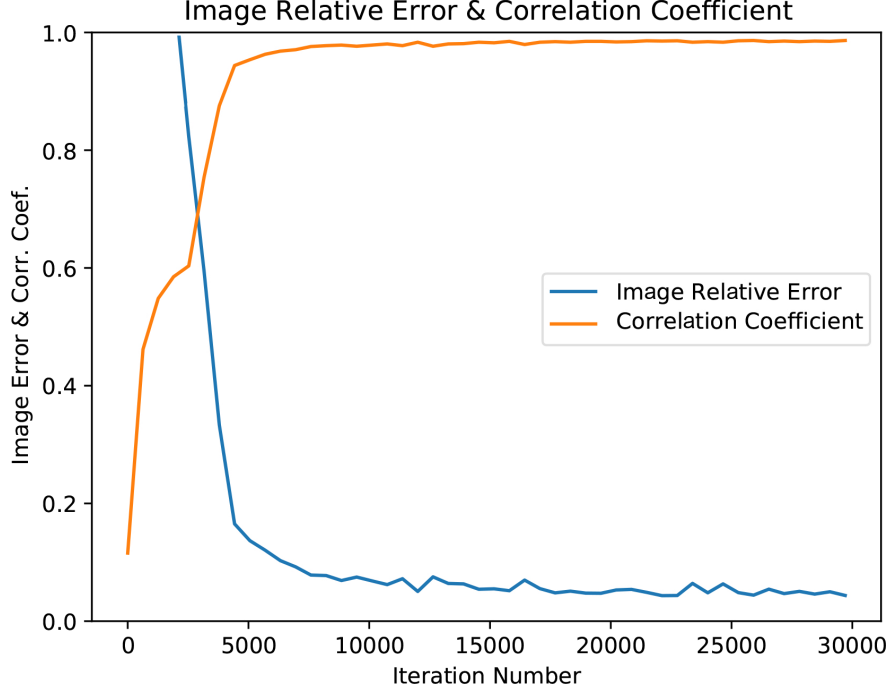
Figure 4: Training and validation loss curves

datasets are quite different, since the dataset for each flow pattern was randomly generated. During the training phase, the testing dataset was applied to the CGAN-ECT model and their values were calculated in each epoch. Fig. 4 shows that the IE curve declines over $30k$ epochs, while the CC curve increases. Both curves approaches their saturation levels, which are 99% and 0.07 for CC and IE, respectively, after about $10k$ epochs.

Table 1: Minimum and maximum of relative IE and CC of testing results

Flow Patterns	Min. IE	Max. IE	Average IE	Min. CC	Max. CC	Average CC
Annular	0.0339	0.1045	0.0593	0.9912	0.9982	0.9957
Ring	0.0425	0.1360	0.0802	0.9835	0.9973	0.9927
Stratified	0.0272	0.0761	0.0484	0.9954	0.9992	0.9973
Single Cir. Bar	0.0457	0.0925	0.0683	0.9887	0.9983	0.9940
Multiple Cir. Bars	0.0448	0.1265	0.0860	0.9841	0.9980	0.9920
Single Sq. Bar	0.0379	0.0843	0.0606	0.9890	0.9979	0.9942
Multiple Sq. Bars	0.0372	0.1344	0.0848	0.9805	0.9982	0.9909
Total Average			**0.0697**			**0.9938**

For quantitative evaluation, the minimum, the maximum, and the average of relative IE and CC are calculated for each two-phase flow patterns group of the testing dataset and shown in Table 1, respectively. The results prove that the proposed CGAN-ECT model has reconstruction capabilities with average CC values more than 99%, and average IE values less than 7%. Box plots of the IE and CC for all flow patterns are drawn in Fig. 5, and Fig. 6, respectively. The upper and lower limits stand for the maximum and minimum of each flow pattern (exact values are given in Table 1), and red line is median.

Examples of reconstructed images for the min. and max. relative image errors of each flow patterns in Table 1 are illustrated in Fig. 7. Visually, reconstructed images which have max. relative IEs are very close to the real flow patterns with small artifacts. The CGAN-ECT model can estimate each object and identify its position in the imaging area of the ECT sensor. On the other hand, the reconstructed images with min. relative IEs have better visual effect. Also, as shown in the Fig. 7, the images with max. relative IE are flow patterns whose low phase ratio, while those whose min. relative IE have high phase ratio, except square bars. In general, the proposed CGAN-ECT model performs well on the
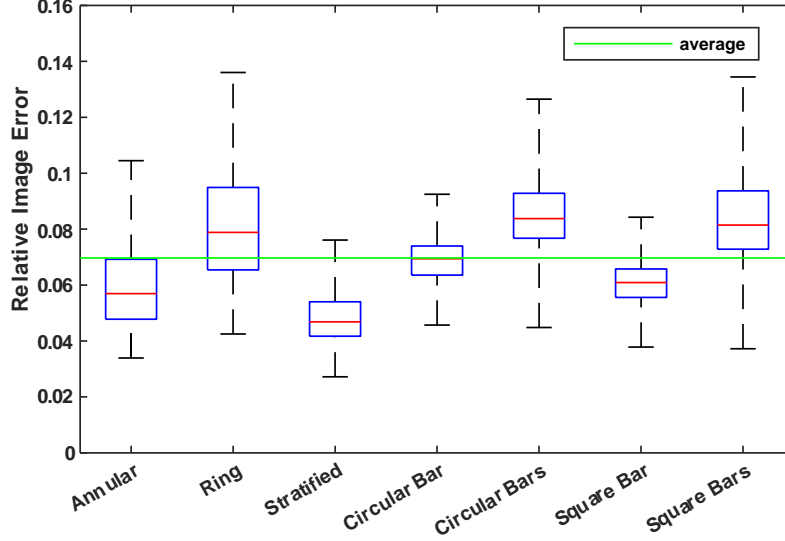
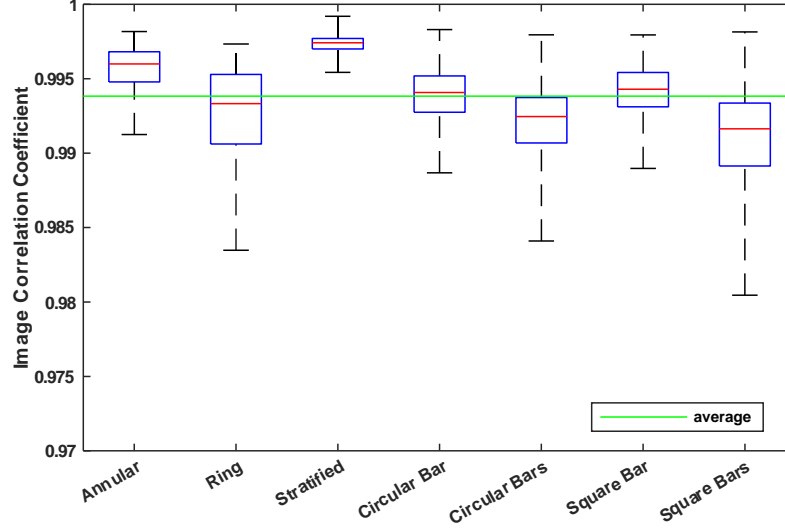Figure 5: Box plots of Relative Image Errors (IE)

Figure 6: Box plots of Correlation Coefficients (CC)

testing dataset and has stronger image reconstruction capabilities for all typical flow patterns with accurately-estimated objects permittivity values.

To test the performance of the proposed CGAN-ECT model, a comparison with other state-of-the-arts ECT image reconstruction algorithms is carried out. The generalization ability of the CGAN-ECT model is examined by applying it to a variety of flow patterns. Fig. 8 illustrates the results where the initial modulated capacitance matrix is shown in the first column, the actual flow pattern is in the second column, the other columns have the reconstructed images from the LBP, iterative Tikhonov, ILM, CNN [27, 28, 29] and CGAN-ECT algorithms, respectively. The iteration number of the Tikhonov algorithm is set to 200 iterations, while the ILM is 1000. The CNN model is trained using the initial images from the LBP algorithm. The results of the CGAN-ECT model have high quality and accuracy with sharp objects' boundaries compared with the reconstructed images from all other algorithms. Visually, it is clear from the results in Fig. 8 that the object edges are sharp, since there is no transition zone between the reconstructed objects by the proposed model compared with the other algorithms. Also, Table 2 contains the IE and CC results of the proposed CGAN-ECT model along with all other algorithms. The values of the IE and CC prove that CGAN-ECT model outperforms the other reconstruction algorithms.
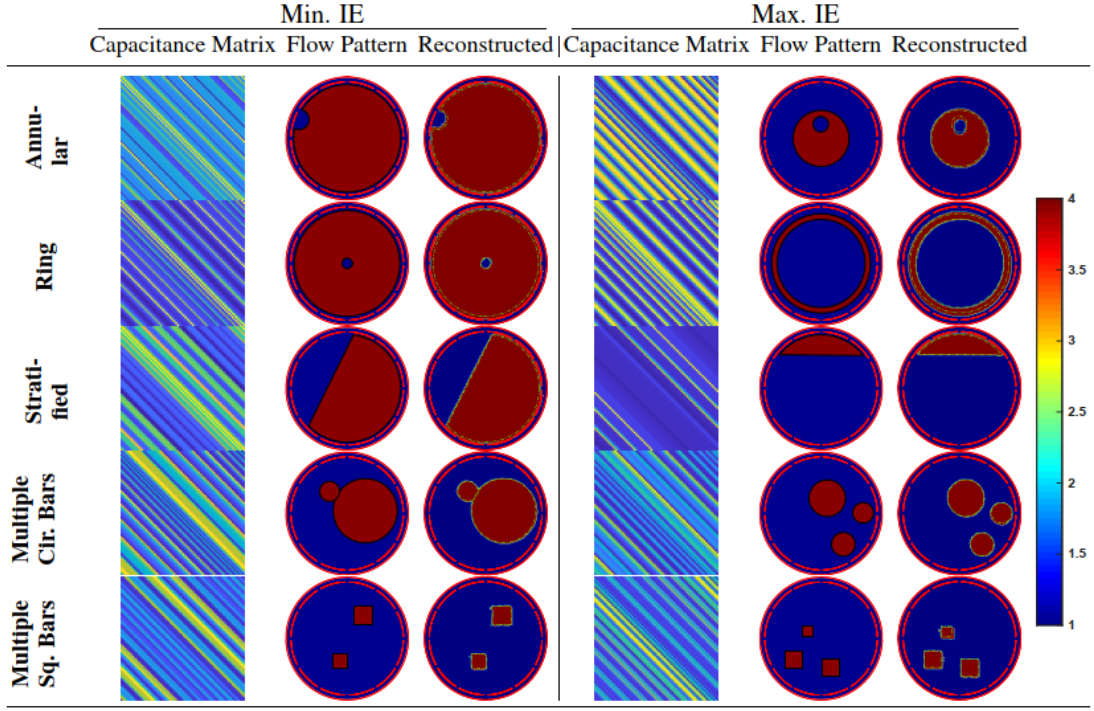
7

Figure 7: Examples of Min. and Max. IE image reconstruction results
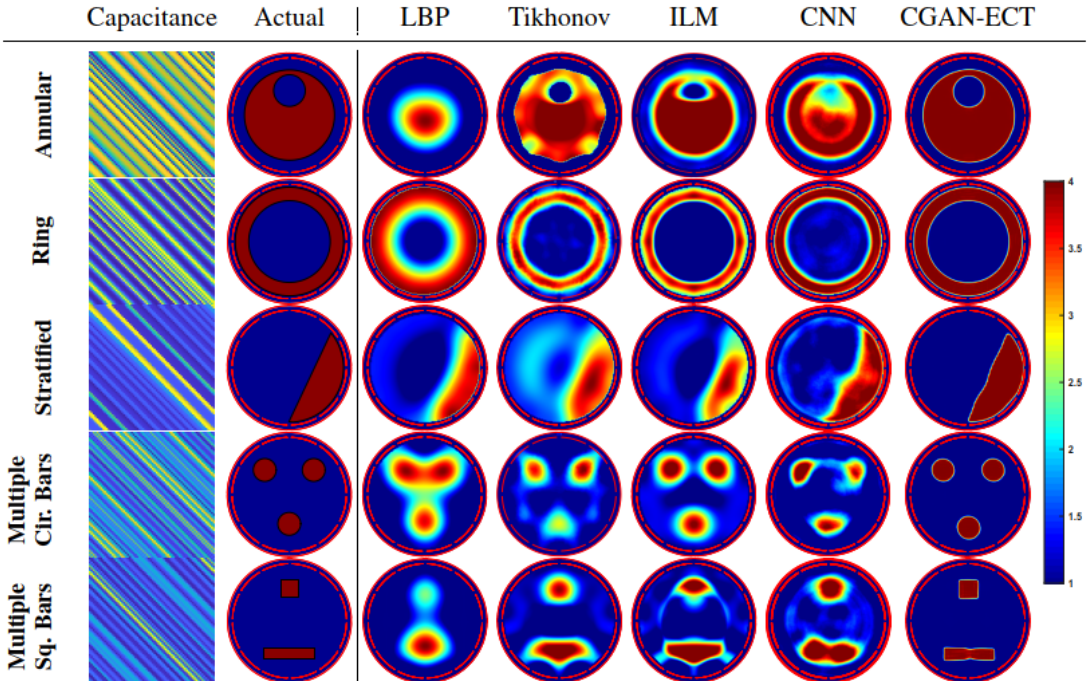

Figure 8: Reconstructed images of different state-of-the-arts image reconstruction algorithms

Table 2: Results of the IE and CC of different ECT image reconstruction algorithms

	Flow	LBP	Tikhonov	ILM	CNN	CGAN-ECT
Relative Image Error	Annular	0.5746	0.3229	0.2693	0.2673	**0.1471**
	Ring	0.3776	0.1216	0.2984	0.2107	**0.0825**
	Stratified	0.2590	0.3793	0.3203	0.2401	**0.1660**
	Multiple Cir. Bars	0.6083	0.7492	0.4275	0.4765	**0.1340**
	Multiple Sq. Bars	0.5236	0.4505	0.4461	0.5933	**0.1586**
Correlation Coefficient	Annular	0.4812	0.8421	0.8648	0.8682	**0.9745**
	Ring	0.8110	0.9792	0.9576	0.9396	**0.9907**
	Stratified	0.9126	0.8518	0.9100	0.9179	**0.9719**
	Multiple Cir. Bars	0.5498	0.5652	0.7625	0.7325	**0.9806**
	Multiple Sq. Bars	0.4572	0.7018	0.7238	0.6915	**0.9571**

Table 3: Results of noise-free and noisy training and testing data

Training Data		Noise-Free		Noisy	
Testing Data		Noise-Free	Noisy	Noise-Free	Noisy
Relative Image Error	Min	0.0385	0.0388	0.0348	0.0351
	Max	0.1078	0.2573	0.1477	0.1829
	Avg.	0.0697	0.1268	0.0854	0.1001
Correlation Coefficient	Min	0.9875	0.9388	0.9773	0.9652
	Max	0.9982	0.9978	0.9983	0.9983
	Avg.	0.9938	0.9775	0.9904	0.9862

3.3.2 Experiments on contaminated data

During the training and testing phases of the CGAN-ECT model, contaminated noisy data was used to test its robustness. Gaussian noise with Signal to Noise Ratio (SNR) equals 30dB was added to the capacitance vectors before the modulation process. The selected SNR is common for most of reported ECT hardware systems. The CGAN-ECT model is trained and tested with noise-free, and noisy datasets. The results of the min., max., and average IE and CC for these two datasets are shown in Table 3. Also, all the results of all different flow patterns groups are stated in Table 4. Statistically, from the results shown in the two tables, there in no big difference when applying noise-free and noisy data. However, the IE and CC values of noise-free training/ noisy testing data are slightly worse than the other models but still substantial.

3.3.3 Results of Nonexistent Flow Patterns in the Training Dataset

The generalization ability of the trained CGAN-ECT model on free-noise data is tested by reconstructing images of flow patterns, which are not included in the training dataset. Four different flow patterns are applied, four circular bars, five square bars, plus shape, and stratified and square bar. The reconstructed images are shown in Fig. 9, and their corresponding relative IE and CC are listed in Table 5. The CGAN-ECT model still can reconstruct the flow patterns with relatively outstanding CC and IE values.

However, the inhomogeneous sensitivity map across ECT cross-sectional sensing domain is a big problem. The CGAN-ECT -generated image of the five square bars proves the ability of the proposed model to reconstruct flow patterns placed in low and high sensitivity areas of the ECT sensor.

Table 4: IE and CC values for noise-free and noisy testing data

| Training Data		Noise-Free		Noisy	
Testing Data		Noise-Free	Noisy	Noise-Free	Noisy
Relative Image Error	Annular	0.0593	0.0747	0.0664	0.0725
	Ring	0.0802	0.1260	0.0899	0.0967
	Stratified	0.0484	0.0655	0.0513	0.0535
	Single Cir. Bar	0.0683	0.1241	0.0749	0.0875
	Multiple Cir. Bars	0.0860	0.1568	0.1047	0.1288
	Single Sq. Bars	0.0606	0.1376	0.0834	0.1008
	Multiple Sq. Bars	0.0848	0.2027	0.1269	0.1610
Correlation Coefficient	Annular	0.9957	0.9932	0.9947	0.9937
	Ring	0.9927	0.9862	0.9912	0.9902
	Stratified	0.9973	0.9952	0.9971	0.9968
	Single Cir. Bar	0.9940	0.9789	0.9929	0.9905
	Multiple Cir. Bars	0.9920	0.9729	0.9884	0.9824
	Single Sq. Bars	0.9942	0.9692	0.9889	0.9836
	Multiple Sq. Bars	0.9909	0.9466	0.9795	0.9663
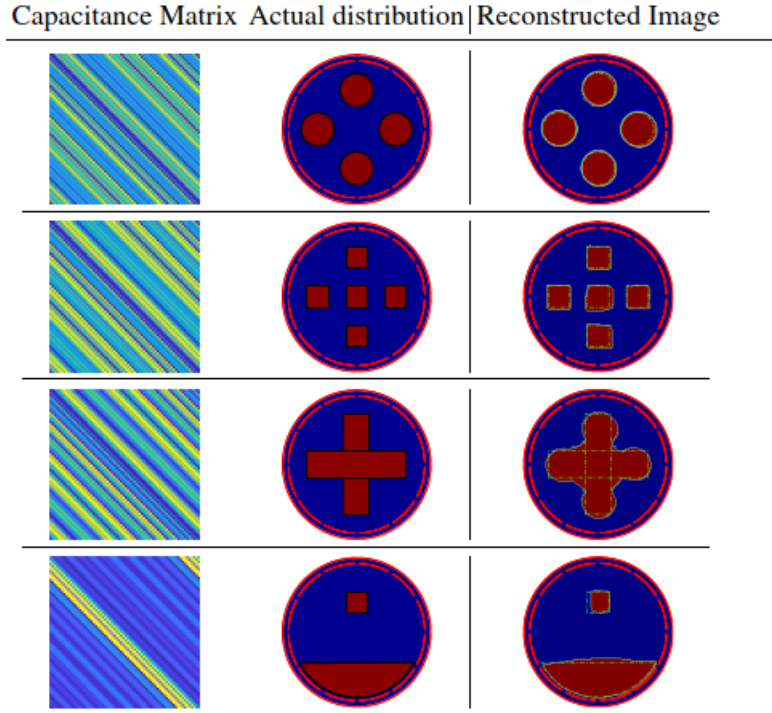
Figure 9: Image reconstruction results of phantoms not in training dataset

Table 5: Results of flow patterns not in training dataset

Phantom	IE	CC
Four Cir. Bars	0.1454	0.9788
Five Sq. Bars	0.2205	0.9499
Plus Shape	0.2534	0.9335
Str. & Square	0.2336	0.9448
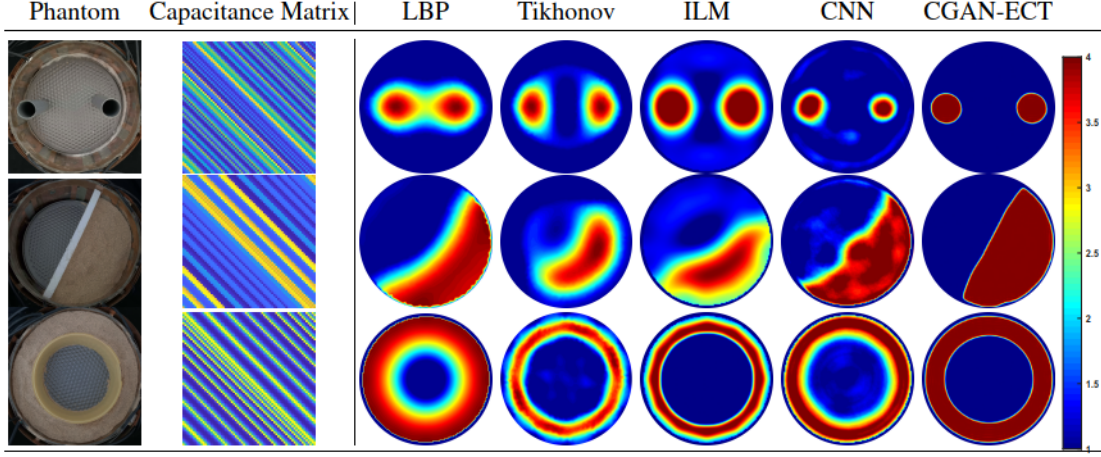
Figure 10: Reconstructed images for real data.

Table 6: Reconstruction time in seconds.

LBP	Tikhonov	ILM	CNN	CGAN-ECT
0.026	5.326	6.245	0.085	0.062

3.3.4 Testing with Real Data

Real experimental data are applied for testing the CGAN-ECT model, which was trained using noise-free data. The measured modulated capacitance matrices of three two-phase flow patterns are used as testing inputs.

The digital Electrical Capacitance Volume Tomography (ECVT) system [30] is used to run the experiment. The ECVT has 36 channels and measures the capacitance between 12 electrodes. The system generates up to 120 images/sec. The experiment is carried out by measuring the capacitance after placing static phantoms in the imaging area. Three flow patterns, circular bars, stratified, and annular are simulated as shown in Fig. 10. The permittivity of the plastic particles is $\epsilon = 4$, while the radius of the plastic rods is $r = 20mm$.

Fig. 10 illustrates real distributions and the generated images from LBP, iterative Tikhonov, CNN, and CGAN-ECT algorithms. The created images from the CGAN-ECT model have high accuracy, few artifacts, and sharp edges between the two phases, when compared with the other four algorithms.

The computational cost is a crucial parameter in the industrial ECT applications. The time costs of the different algorithms are listed in Table 6. The calculations are carried out using a PC with an i9 CPU (3.6 GHz) and 64 GB memory. The CGAN-ECT model is faster and constructs high quality images compared to three out of the four other algorithms. Although the LBP is faster than CGAN-ECT , the image quality is much lower, the case which gives logical preference to scarifying little more reconstruction time for much better accuracy.

4 Conclusions

In this paper, a novel ECT image reconstruction model using CGAN deep neural network was developed to reconstruct ECT images from capacitance measurements. A large-scaled ECT dataset of $320k$ instants data was created to train and test the proposed model. The generalization, robustness, and performance of the CGAN-ECT model are evaluated based on contaminated noisy data, flow patterns that were not included the training dataset, and experimental real data. Experimental results show that the proposed model produces satisfying visual quality. Quantitatively, CGAN-ECT achieved average image correlation coefficient above 99% and average relative image error below 0.07. These quantitative results prove that CGAN-ECT outperforms state-of-the-arts algorithms, specifically LBP, iterative Tikhonov, ILM and CNN methods. On the efficiency side, CGAN-ECT achieved better computational cost than the state-of-the-arts in most cases and slightly worse in one case whose accuracy is far below that of CGAN-ECT .

References

[1] AV Korjenevsky. Electric field tomography for contactless imaging of resistivity in biomedical applications. *Physiological measurement*, 25(1):391, 2004.

[2] Mi Wang. *Industrial tomography: systems and applications*. Elsevier, 2015.

[3] Haigang Wang and Wuqiang Yang. Scale-up of an electrical capacitance tomography sensor for imaging pharmaceutical fluidized beds and validation by computational fluid dynamics. *Measurement Science and Technology*, 22(10):104015, sep 2011.

[4] Tomasz Rymarczyk, Grzegorz Kłosowski, and Arkadiusz Gola. The use of artificial neural networks in tomographic reconstruction of soil embankments. In *International Symposium on Distributed Computing and Artificial Intelligence*, pages 104–112. Springer, 2018.

[5] Tomasz Rymarczyk, Grzegorz Kłosowski, and Edward Kozłowski. A non-destructive system based on electrical tomography and machine learning to analyze the moisture of buildings. *Sensors*, 18(7):2285, 2018.

[6] Wan Norhisyam Abd Rashid, Elmy Johana Mohamad, Ruzairi Abdul Rahim, Jaafar Abdullah, and Hanis Liyana Mohmad Ameran. Electrical capacitance tomography: a review on portable ECT system and hardware design. *Sensor Review*, 36(1):64–70, 2016.

[7] Chan Kok Seong, Jaysuman Pusppanathan, Ruzairi Abdul Rahim, Goh Chiew Loon, Yvette Shaan Li Susiapan, Fatin Aliah Phang, and Mohd Hafiz Fazalul Rahiman. Hardware development of electrical capacitance tomography (ECT) system with capacitance sensor for liquid measurements. *Jurnal Teknologi*, 73(6), 2015.

[8] Ziqiang Cui, Qi Wang, Qian Xue, Wenru Fan, Lingling Zhang, Zhang Cao, Benyuan Sun, and Huaxiang Wang. A review on image reconstruction algorithms for electrical capacitance / resistance tomography. *Sensor Review*, 36(4):429–445, 2016.

[9] Sigeru Omatu, Ali Selamat, Grzegorz Bocewicz, Paweł Sitek, Izabela Nielsen, Julián A. García-García, and Javier Bajo. Preface. In *Advances in Intelligent Systems and Computing*, volume 474, pages V–VI, 2016.

[10] JC Gamio, Carlos Ortiz-Aleman, and Roland Martin. Electrical capacitance tomography two-phase oil-gas pipe flow imaging by the linear back-projection algorithm. *Geofísica Internacional*, 44(3):265–273, 2005.

[11] M. Vauhkonen, D. Vadâsz, P. A. Karjalainen, E. Somersalo, and J. P. Kaipio. Tikhonov regularization and prior information in electrical impedance tomography. *IEEE Transactions on Medical Imaging*, 17(2):285–293, 1998.

[12] De-yun Chen, Yu Chen, Li-li Wang, and Xiao-yang YU. A novel gauss-newton image reconstruction algorithm for electrical capacitance tomography system [j]. *Acta Electronica Sinica*, 4(37):739–743, 2009.

[13] Yi Li and Wuqiang Yang. Image reconstruction by nonlinear landweber iteration for complicated distributions. *Measurement Science and Technology*, 19(9):094014, 2008.

[14] Hai Zhu, Jiangtao Sun, Jun Long, Wenbin Tian, Shijie Sun, and Lijun Xu. Deep image refinement method by hybrid training with images of varied quality in electrical capacitance tomography. *IEEE Sensors Journal*, 21(5):6342–6355, 2021.

[15] Q. Marashdeh, W. Warsito, L-S Fan, and F. L. Teixeira. A nonlinear image reconstruction technique for ECT using a combined neural network approach. *Measurement Science and Technology*, 17(8):2097–2103, 2006.

[16] Wael Deabes, Alaa Sheta, and Malik Braik. Ect-lstm-rnn: An electrical capacitance tomography model-based long short-term memory recurrent neural networks for conductive materials. *IEEE Access*, 9:76325–76339, 2021.

[17] Wael Deabes and Khalid M Jamil Khayyat. Image reconstruction in electrical capacitance tomography based on deep neural networks. *IEEE Sensors Journal*, 2021.

[18] Hai Zhu, Jiangtao Sun, Lijun Xu, Wenbin Tian, and Shijie Sun. Permittivity reconstruction in electrical capacitance tomography based on visual representation of deep neural network. *IEEE Sensors Journal*, 20(9):4803–4815, 2020.

[19] Wael Deabes, Alaa E. Abdel-Hakim, Kheir Eddine Bouazza, and Hassan Althobaiti. Adversarial resolution enhancement for electrical capacitance tomography image reconstruction. *Sensors*, 22(9), 2022.

[20] Wael Deabes and Kheir Eddine Bouazza. Residual autoencoder deep neural network for electrical capacitance tomography. *Computers, Materials & Continua*, 73:6307–6326, 01 2022.

[21] Mehdi Mirza and Simon Osindero. Conditional generative adversarial nets. *arXiv preprint arXiv:1411.1784*, 2014.

[22] Olaf Ronneberger, Philipp Fischer, and Thomas Brox. U-net: Convolutional networks for biomedical image segmentation. In *International Conference on Medical image computing and computer-assisted intervention*, pages 234–241. Springer, 2015.

[23] Alec Radford, Luke Metz, and Soumith Chintala. Unsupervised representation learning with deep convolutional generative adversarial networks. *arXiv preprint arXiv:1511.06434*, 2015.

[24] øyvind Isaksen. A review of reconstruction techniques for capacitance tomography. *Measurement Science and Technology*, 7(3):325–337, 3 1996.

[25] Martín Abadi et al. TensorFlow: Large-scale machine learning on heterogeneous systems, 2015. Software available from tensorflow.org.

[26] Francois Chollet et al. Keras, 2015.

[27] Jin Zheng, Haocheng Ma, and Lihui Peng. A CNN-based image reconstruction for electrical capacitance tomography. In *Proceedings of IEEE International Conference on Imaging Systems and Techniques, IST*, pages 1–6. IEEE, 2019.

[28] Wang Lili, Liu Xiao, Chen Deyun, Yang Hailu, and Chengdong Wang. ECT Image Reconstruction Algorithm Based on Multiscale Dual-Channel Convolutional Neural Network. *Complexity*, 2020, 2020.

[29] Chao Tan, Shuhua Lv, Feng Dong, and Masahiro Takei. Image Reconstruction Based on Convolutional Neural Network for Electrical Resistance Tomography. *IEEE Sensors Journal*, 19(1):196–204, jan 2019.

[30] Tech4Imaging LLC. Electrical capacitance volume tomography, Aug 2020.